Available online at www.sciencedirect.com
ScienceDirect
Trans. Nonferrous Met. Soc. China 32(2022) 3149−3162
Transactions of Nonferrous Metals Society of China
www.tnmsc.cn

Facile fabrication of spherical flower-like $Mg(OH)_2$ and its fast and efficient removal for heavy metal ions

Xiao-yi SHEN[1,2], Yan-xiang HUANG[1], Hong-mei SHAO[3],
Yuan WANG[1], Qing HAN[1], Jian-she CHEN[1], Bin-chuan LI[1], Yu-chun ZHAI[1]

1. Key Laboratory for Ecological Metallurgy of Multimetallic Mineral (Ministry of Education), School of Metallurgy, Northeastern University, Shenyang 110819, China;
2. Liaoning Key Laboratory for Metallurgical Sensor and Technology, Northeastern University, Shenyang 110819, China;
3. School of Environmental and Chemical Engineering, Shenyang Ligong University, Shenyang 110159, China

Received 9 August 2021; accepted 21 March 2022

Abstract: Spherical flower-like $Mg(OH)_2$ was fabricated from $MgSO_4$ effluent and its adsorption performance for heavy metal ions was evaluated. The appropriate fabrication conditions are as follows: Mg^{2+}/NH_4OH molar ratio of 1:0.5, temperature of 120 °C and time of 1 h at Mg^{2+} concentration of 2 mol/L. Spherical flower-like $Mg(OH)_2$ composed of ultra-thin sheets exhibits an excellent adsorption ability for Ni^{2+}, Cu^{2+}, Zn^{2+}, Pb^{2+}, Fe^{3+} and Co^{2+}, and the adsorption reaches the equilibrium in 6 min. The maximum adsorption capacities of the studied heavy metal ions onto $Mg(OH)_2$ at 20 °C are 58.55, 85.84, 44.94, 485.44, 625.00 and 27.86 mg/g, respectively. The adsorption is well fitted by the Langmuir model, indicating that the adsorption is monolayer. The adsorption kinetics follows the pseudo-second-order model. Chemisorption is the operative mechanism. Spherical flower-like $Mg(OH)_2$ is a qualified candidate for heavy metal ions removal.

Key words: $MgSO_4$ effluent; flower-like $Mg(OH)_2$; heavy metal ion; adsorption

1 Introduction

Water, identified as the source of life, is being threatened by various pollutants due to the rapid industrial development. Among the pollutants, heavy metal ions are not easily degradable and can cause ecologic problems if being directly released into water bodies [1,2]. Therefore, it is essential to remove the heavy metal ions from the industrial effluents before being discharged. To date, many methods have been developed to remove the heavy metal ions, including chemical precipitation, membrane separation, adsorption, ion exchange and so on [2−4]. Among them, adsorption using inorganic absorbents is one of the promising ways for its simplicity, high efficiency and easy operation [2,3]. However, the adsorption efficiency critically depends on absorbents. The production cost and recycling performance also affect its application. Generally, the morphology and size of micro/nano-structured adsorbents determine their properties [1]. The controllable synthesis of micro/nano-structures with desirable morphologies has been paid much attention. The hydrothermal method is widely used owning to its simplicity, high yield, good repeatability and controllability [5].

$Mg(OH)_2$ with special morphology exhibits a great prospect in toxic wastewater treatment. As an adsorbent, it has the advantages of nontoxic, noncorrosive and environmental friendly. However, the commonly used raw materials are analytic

Corresponding author: Xiao-yi SHEN, Tel: +86-24-83687731, E-mail: shenxy@smm.neu.edu.cn
DOI: 10.1016/S1003-6326(22)66010-2

chemicals, and in order to obtain $Mg(OH)_2$ with special morphology, we usually need the help of surfactants [6−8]. Few reports are available in the synthesis of $Mg(OH)_2$ with special morphology and excellent adsorption performance from industrial effluent aiming at improving the resource utilization efficiency and environmental sustainability, for example, $MgSO_4$ effluent in laterite hydrometallurgy. Thus, a facile, fast and surfactant-free method is still required in low-cost and large-scale fabrication of $Mg(OH)_2$ with special morphology.

In this study, flower-like $Mg(OH)_2$ was synthesized using $MgSO_4$ effluent via a surfactant-free hydrothermal method. And the influences of Mg^{2+}/NH_4OH molar ratio, hydrothermal temperature, time and Mg^{2+} concentration were discussed in detail. The crystal structures and morphologies of $Mg(OH)_2$ were identified and observed using X-ray diffraction (XRD) and scanning electric microscopy (SEM). The adsorption performance of flower-like $Mg(OH)_2$ for Ni^{2+}, Cu^{2+}, Zn^{2+}, Pb^{2+}, Fe^{3+} and Co^{2+} was studied under varied operating parameters. The isotherm study was carried out using the non-linear Langmuir and Freundlich models. Furthermore, the adsorption thermodynamics was discussed. Finally, the adsorption mechanism was determined.

2 Experimental

2.1 Materials

$MgSO_4$ solution (containing $(NH_4)_2SO_4$) obtained from laterite hydrometallurgy after mixing (with $(NH_4)_2SO_4$), roasting, water leaching and purification (precipitating Fe^{3+} as ammonium jarosite and Al^{3+} as $Al(OH)_3$ using NH_4HCO_3, precipitating Ni^{2+} as NiS using Na_2S solution) was used as raw material. And Mg^{2+} concentration was adjusted to a range of 1.5−2.5 mol/L. Analytic NH_4OH was employed as precipitant. The nickel laterite (from Huili, Sichuan Province, China) contained NiO with a grade of 0.99%, Fe_2O_3 with a content of 13.62% (existing as hematite and magnetite), SiO_2 with a grade of 44.83% (existing as quartz, lizardite and clinochrysotile), Al_2O_3 with a content of 3.54% (existing as silicate), and MgO with a content of 34.02% (exists as lizardite and clinochrysotile). Cobalt and calcium were in a low level.

2.2 Experimental procedure

2.2.1 Preparation of flower-like $Mg(OH)_2$

$MgSO_4$ solution ranging from 1.5 to 2.5 mol/L and 2.0 mol/L NH_4OH solution were mixed at desirable Mg^{2+}/NH_4OH molar ratio within 1:0.4 to 1:0.6 and magnetically stirred for 30 min at 40 °C. Then, the mixed solution was added into a 200 mL Teflon lined autoclave and placed in a pre-heated oven ranging from 80 to 140 °C keeping for within 3 h. Afterwards, the autoclave was cooled down. The slurry was filtered and the specimen was washed repeatedly by distilled water and three times by ethanol before being dried at 80 °C.

2.2.2 Adsorption test

The adsorption experiments were carried out in batches with fixed volume of 50 mL and stirring speed of 300 r/min for a given time. Then, the solution was filtered before measuring. The masses of $Mg(OH)_2$ varied in 50−300 mg (Cu^{2+}, Zn^{2+}), 100−600 mg (Ni^{2+}, Co^{2+}), 10−20 mg (Fe^{3+}) and 10−80 mg (Pb^{2+}) were studied to determine the optimal dosage (300, 200, 250, 60, 20 and 600 mg for Ni^{2+}, Cu^{2+}, Zn^{2+}, Pb^{2+}, Fe^{3+} and Co^{2+}, respectively). The initial ion concentration of 200 mg/L was used for adsorption time tests at 20 °C and initial solution pH (6.21, 5.14, 5.91, 4.62, 2.95 and 5.95 for $NiCl_2$, $CuCl_2$, $ZnCl_2$, $PbCl_2$, $FeCl_3$ and $CoCl_2$, respectively, tested by Leici PHSJ-4F pH meter). As for ion concentration study, the adsorption along with ion concentration varied from 100 to 500 mg/L was discussed assuming no precipitate. As for the pH study, the solution pH was adjusted using HCl and NaOH solutions (0.1 mol/L).

2.2.3 Characterization

The structures of $Mg(OH)_2$ specimens was identified using a Japan Rigaku Ultima IV X-ray diffractometer, employing Cu K_α radiation with a voltage 40 kV, at a scanning rate of 6 (°)/min with 2θ ranging from 5° to 90°. The morphologies of the $Mg(OH)_2$ specimens were observed by a Japan Hitachi 8010 scanning electron microscope. The concentrations of those heavy metal ions were measured using a TAS−990 atom adsorption spectrophotometer.

2.3 Zero point of charge (pH_{zpc})

The pH_{zpc} was determined by adding 100 mg $Mg(OH)_2$ into 100 mL of 0.1 mg/L $NaNO_3$ solution within the initial pH ranging from 4 to 12, shaking for 24 h and measuring the equilibrium pH values of the solutions after separation. The difference of equilibrium and initial pH (pH_e–pH_i) as a function of initial pH was obtained, and the point at which the curve intersected the *x*-axis was pH_{zpc} [9].

2.4 Adsorption isotherms

The experimental data of heavy metal ions adsorption were fitted using non-linear Langmuir model (Eq. (1)) and Freundlich model (Eq. (2)) [10−15]:

$$q_e = \frac{K_L q_{max} C_e}{1 + K_L C_e} \tag{1}$$

$$q_e = K_F C_e^{1/n} \tag{2}$$

where C_e is the equilibrium concentration of ions in the solution (mg/L), q_e is the equilibrium capacity of ions on the adsorbent (mg/g), q_{max} is the maximum adsorption capacity (mg/g), K_L is the Langmuir adsorption constant (L/mg) related to the free energy of adsorption, K_F is the constant dependent on adsorption capacity and adsorption strength ($mg^{1-1/n}\cdot g^{-1}\cdot L^{-1/n}$), and $1/n$ is Freundlich constant and large n is characterization of better adsorption.

2.5 Adsorption thermodynamics

Thermodynamic parameters of the adsorption process were calculated from the adsorption isotherms using Eqs. (3) and (4), including standard free energy change (ΔG^{Θ}), enthalpy change (ΔH^{Θ}) and entropy change (ΔS^{Θ}) [11−17]:

$$\Delta G^{\Theta} = -RT \ln K_c \tag{3}$$

$$\ln K_c = \frac{\Delta S^{\Theta}}{R} - \frac{\Delta H^{\Theta}}{RT} \tag{4}$$

where K_c is the equilibrium constant of adsorption, T is the thermodynamic temperature and R is the molar gas constant.

2.6 Adsorption kinetics

Adsorption kinetics of Ni^{2+}, Cu^{2+}, Zn^{2+}, Pb^{2+}, Fe^{3+} and Co^{2+} by $Mg(OH)_2$ were evaluated by pseudo-first-order (Eq. (5)) and pseudo-second-order (Eq. (6)) models [11−17], and also fitted by intra-particle diffusion model (Eq. (7)) [13−15]:

$$\ln(q_e - q_t) = \ln q_e - k_1 t \tag{5}$$

$$\frac{t}{q_t} = \frac{1}{k_2 q_e^2} + \frac{t}{q_e} \tag{6}$$

where t is time (min), q_t (mg/g) is the adsorption capacity of ions at time t, k_1 (min^{-1}) and k_2 ($g\cdot mg^{-1}\cdot min^{-1}$) are the pseudo-first-order and pseudo-second-order rate constants, respectively.

$$q_t = kt^{1/2} + C \tag{7}$$

where k is the intraparticle diffusion rate constant ($mg\cdot g^{-1}\cdot min^{-1/2}$), and C is the film thickness.

3 Results and discussion

3.1 Influences of operating parameters on structures and morphologies of $Mg(OH)_2$

3.1.1 Influence of Mg^{2+}/NH_4OH molar ratio

The effect of Mg^{2+}/NH_4OH molar ratio on the structures and morphologies of $Mg(OH)_2$ was studied under Mg^{2+} concentration of 2.0 mol/L, temperature of 120 °C and time of 1 h. The XRD study indicates Mg^{2+}/NH_4OH molar ratio has no effect on $Mg(OH)_2$ structure. All diffraction data are in good agreement with JCPDS No. 441482. No other characteristic peak is detected, indicating that the obtained $Mg(OH)_2$ has hexagonal structure with regular crystal form and high purity. Molar ratio has an obvious effect on the morphology of $Mg(OH)_2$. When Mg^{2+}/NH_4OH molar ratio is in the range from 1:0.4 to 1:0.5, the obtained $Mg(OH)_2$ exhibits uniform and regular flower-like structures composed of lots of ultra-thin sheets (Figs. 1(b, c)), which are distributed in a narrow range. Increasing the NH_4OH dosage, a large number of crystal nuclei formed in the initial stage kinetically grow into large crystals, resulting in structure destruction. Furthermore, agglomeration is observed (Fig. 1(d)). Molar ratio of 1:0.5 was chosen in the following experiments.

3.1.2 Influence of reaction temperature

Figure 2 shows the XRD patterns and SEM images of $Mg(OH)_2$ obtained at different temperatures ranging from 80 to 140 °C under conditions of Mg^{2+}/NH_4OH ratio of 1:0.5, Mg^{2+} concentration of 2.0 mol/L and time of 1 h. The reaction temperature has no obvious effect on the structure of $Mg(OH)_2$ (Fig. 2(a)), but has a significant effect on the morphology of $Mg(OH)_2$. Although $Mg(OH)_2$ specimens obtained at 80 and 100 °C display flower-like structures (Figs. 2(b, c)), the irregular and incomplete structures and flaky particles are observed. High temperature facilitates

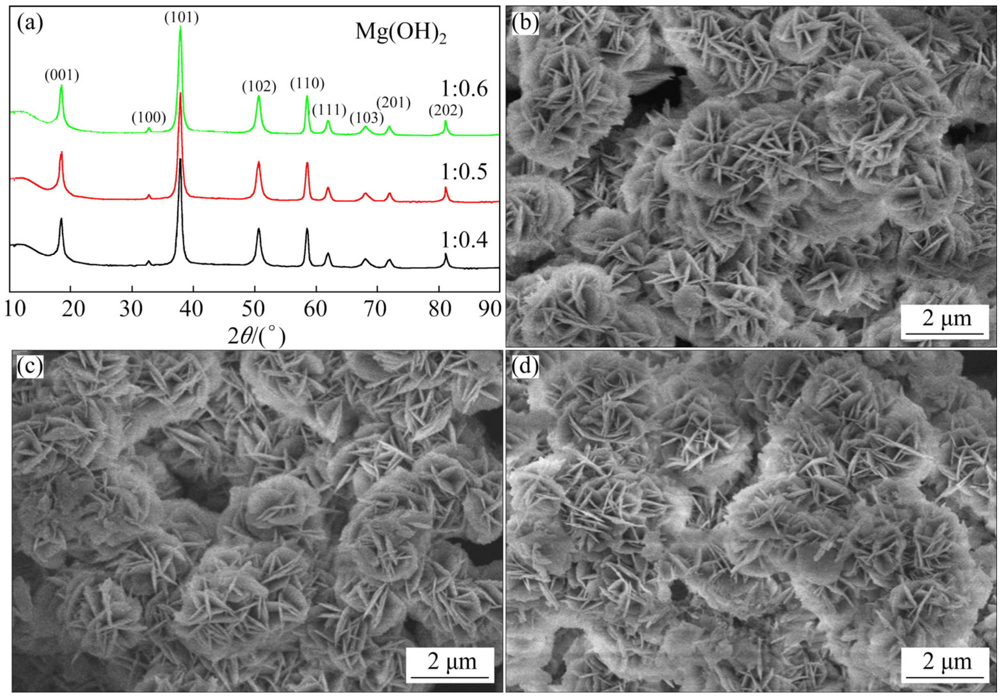

Fig. 1 XRD patterns (a) and SEM images of flower-like $Mg(OH)_2$ obtained at Mg^{2+}/NH_4OH molar ratios of 1:0.4 (b), 1:0.5 (c) and 1:0.6 (d)

the regular growth of $Mg(OH)_2$ crystals to form the uniform flower-like structure (Fig. 2(d)). However, when the temperature reaches 140 °C, the particle size grows obviously from 2 to 2.5−3.0 μm, and the edges of ultra-thin sheets become blurry owning to the hydration of $Mg(OH)_2$ [18], which may have a negative effect on the adsorption due to decreasing the specific surface area. Temperature of 120 °C was selected in subsequent experiments.

3.1.3 Influence of reaction time

The influence of reaction time on the structures and morphologies of $Mg(OH)_2$ was also examined under condition of Mg^{2+}/NH_4OH ratio of 1:0.5, Mg^{2+} concentration of 2.0 mol/L and temperature of 120 °C, and the results are shown in Fig. 3. All the obtained $Mg(OH)_2$ specimens have hexagonal structure. Obviously, a longer reaction time disrupts the flower-like structure, even causing the agglomeration (Fig. 3(d)). The flower-like structures become irregular and the edges of the ultra-thin sheets are indistinct. This is due to the hydration of $Mg(OH)_2$ under hydrothermal conditions. $Mg(OH)_2$ obtained at 1 h presents a uniform and regular morphology (Fig. 3(b)). It can be said that 1 h is appropriate for the fabrication of flower-like $Mg(OH)_2$.

3.1.4 Influence of Mg^{2+} concentration

Figure 4 shows the XRD patterns and SEM images of $Mg(OH)_2$ obtained at different Mg^{2+} concentrations under conditions of 120 °C, 1 h and Mg^{2+}/NH_4OH ratio of 1:0.5. The results displayed in Fig. 4 indicate that all the obtained specimens are hexagonal-structure $Mg(OH)_2$. Increasing Mg^{2+} concentration, flower-like $Mg(OH)_2$ grows more uniformly and regularly with a size of about 2 μm (Fig. 3(b)). However, a high level of 2.5 mol/L results in the agglomeration of $Mg(OH)_2$ particles. And the edges of ultra-thin sheets become blurry (Fig. 4(c)). This may be attributed to the formation of a large number of crystal nuclei in the initial growth stage, which kinetically grow into large crystals. Excessive crystals disorder the regular flower-like structure. The 2.0 mol/L of $MgSO_4$ solution was chosen.

The main elements in EDS pattern (Fig. 4(d)) are Mg and O with an molar ratio close to 2:1 (from flower-like $Mg(OH)_2$) and Au (from the gold spraying for imaging), confirming that $Mg(OH)_2$ is pure. The flower-like structure and the space between ultra-thin sheets provide a high specific surface area of 42.4 m^2/g, a total pore volume by BJH method of 0.10 cm^3/g, a half-pore size of 20.37 nm and tunnels for the transport of heavy metal ions, which is favourable for adsorption [11].

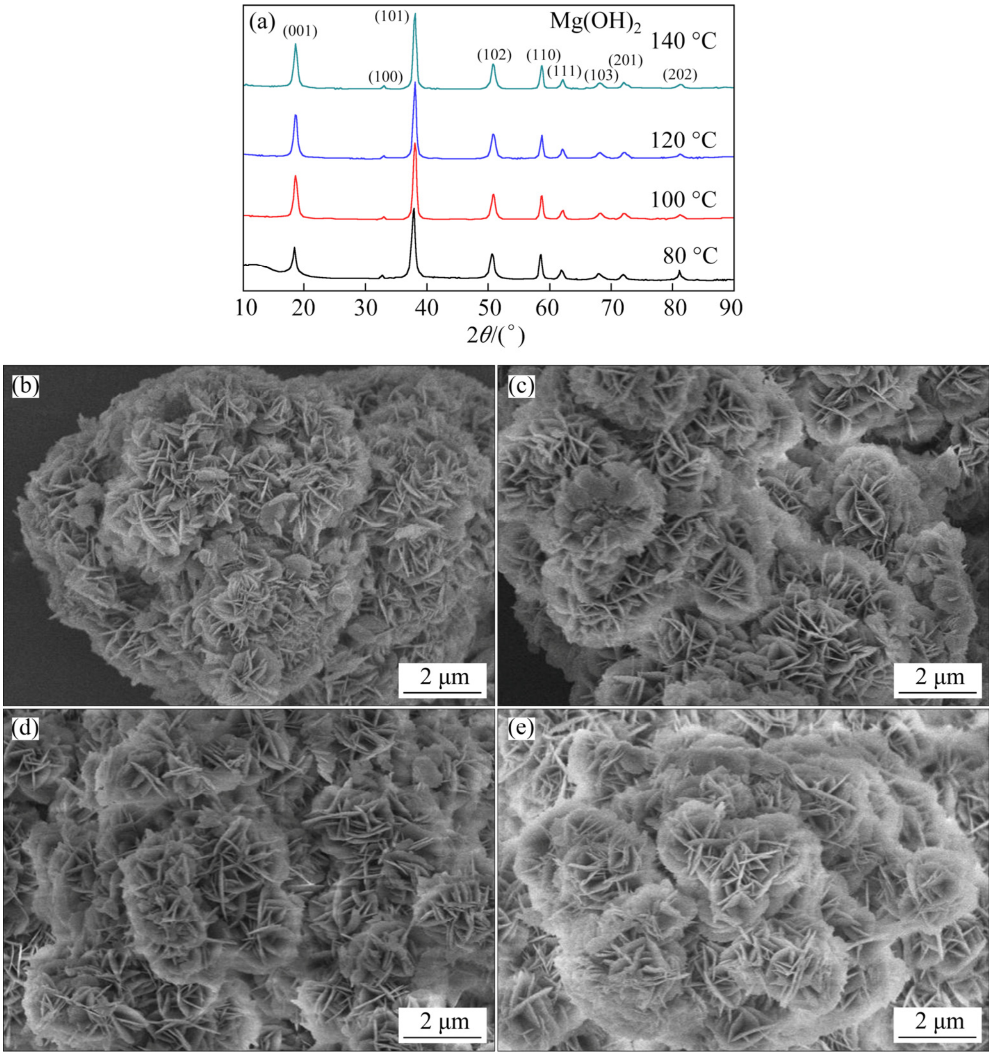

Fig. 2 XRD patterns (a) and SEM images of flower-like $Mg(OH)_2$ obtained at 80 °C (b), 100 °C (c), 120 °C (d) and 140 °C (e)

3.2 Growth mechanism of flower-like $Mg(OH)_2$

Nucleation and crystal growth are the two main stages in crystal formation. The growth process of flower-like $Mg(OH)_2$ under hydro-thermal condition is a process of dissolution and recrystallization. Due to the rapid nucleation, a large number of $Mg(OH)_2$ nuclei are formed and grow into tiny crystals because of the surface energy effect. And the tiny crystals kinetically favor to grow into the large crystals in supersaturated solution. In the hexagonal system, the energy is minimal when the crystal grows along the (001) plane. However, the hydrothermal environment can provide a driving force for (101) plane growth. And crystals growth in the direction of (101) would preferentially proceed under relatively low temperature [19]. Furthermore, LV et al [20] pointed out that the concentration ratio of Mg^{2+} to OH^- was the key factor and decided the preferred growth orientation. A low coordination number of Mg^{2+} ion means that the (101) plane is a stable and preferred orientation plane [20]. The growth of flower-like $Mg(OH)_2$ is schematically presented in Fig. 5.

3.3 Adsorption of heavy metal ions on $Mg(OH)_2$

3.3.1 Influence of adsorption time

The adsorption capacities (q_t) of flower-like $Mg(OH)_2$ for Ni^{2+}, Cu^{2+}, Zn^{2+}, Pb^{2+}, Fe^{3+} and Co^{2+} versus adsorption time are presented in Fig. 6(a). High adsorption capacities are achieved in 1 min for Ni^{2+}, Pb^{2+}, Fe^{3+} and Co^{2+}, indicating that high removal ratios are achieved. The adsorption capacity of Fe^{3+} is astonishingly high, followed by

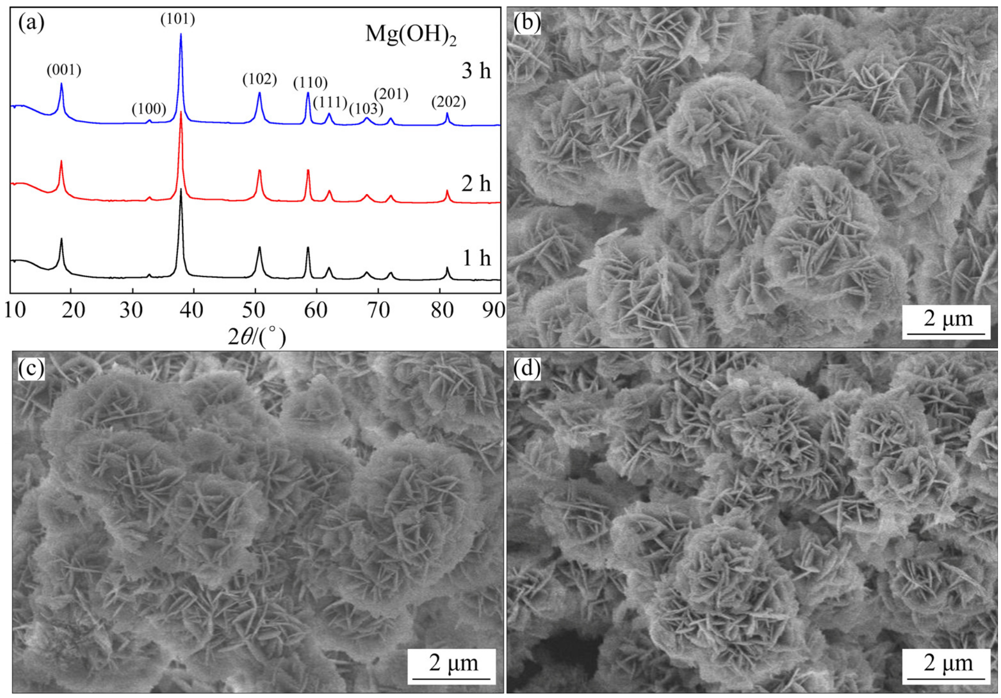

Fig. 3 XRD patterns (a) and SEM images of $Mg(OH)_2$ obtained at 1 h (b), 2 h (c) and 3 h (d)

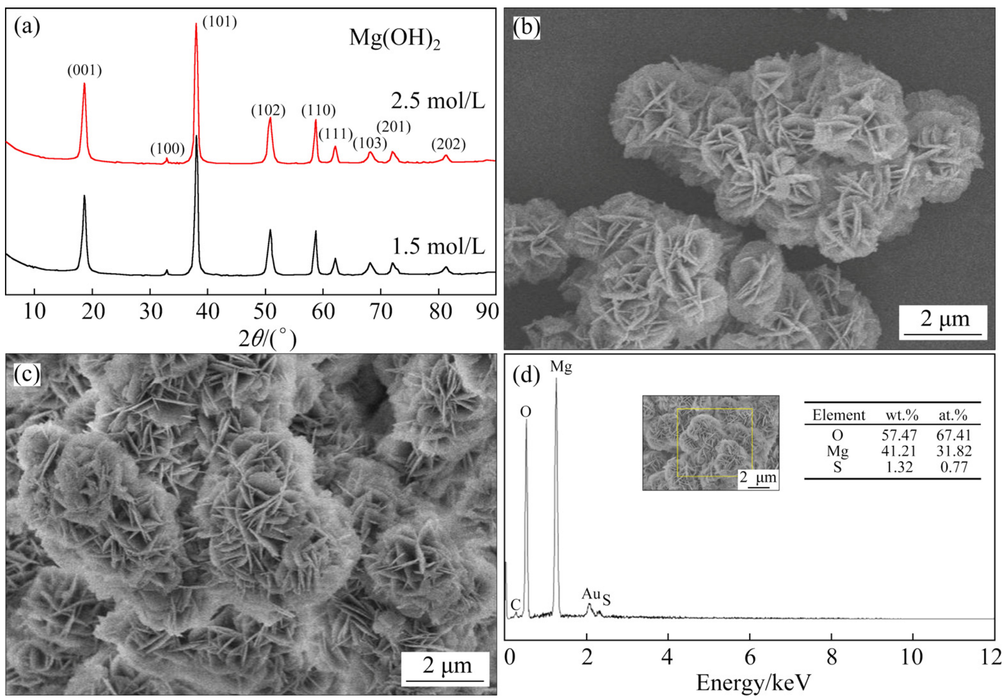

Fig. 4 XRD patterns (a), SEM images obtained at varied Mg^{2+} concentrations of 1.5 mol/L (b) and 2.5 mol/L (c), and EDS pattern of flower-like $Mg(OH)_2$ (d)

Pb^{2+}. One possible reason is that iron has the strongest tendency to hydrolyze due to the addition of basic $Mg(OH)_2$. The adsorption basically reaches equilibrium in 6 min, and the rapid and efficient removal is its advantage in practical application. Consistently, it can be calculated that the removal of these heavy metal ions studied is closed to 100%.

3.3.2 Influence of initial ions concentration

Another important parameter affecting the adsorption is initial ion concentration, which can provide the driving force to overcome the resistance between two phases. The adsorption capacities (q_e)

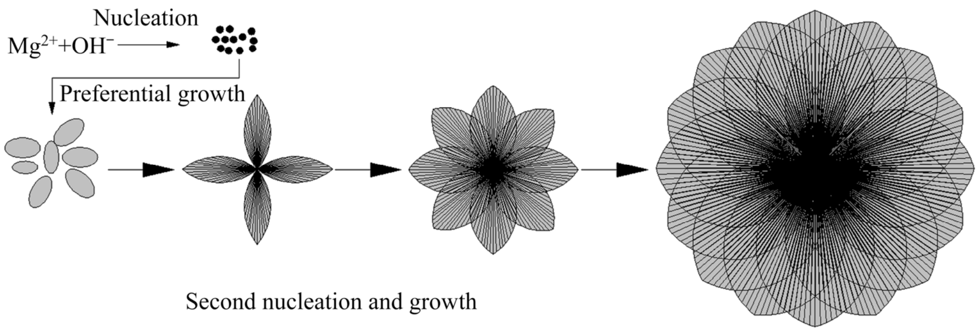

Fig. 5 Schematic growth diagram of flower-like $Mg(OH)_2$

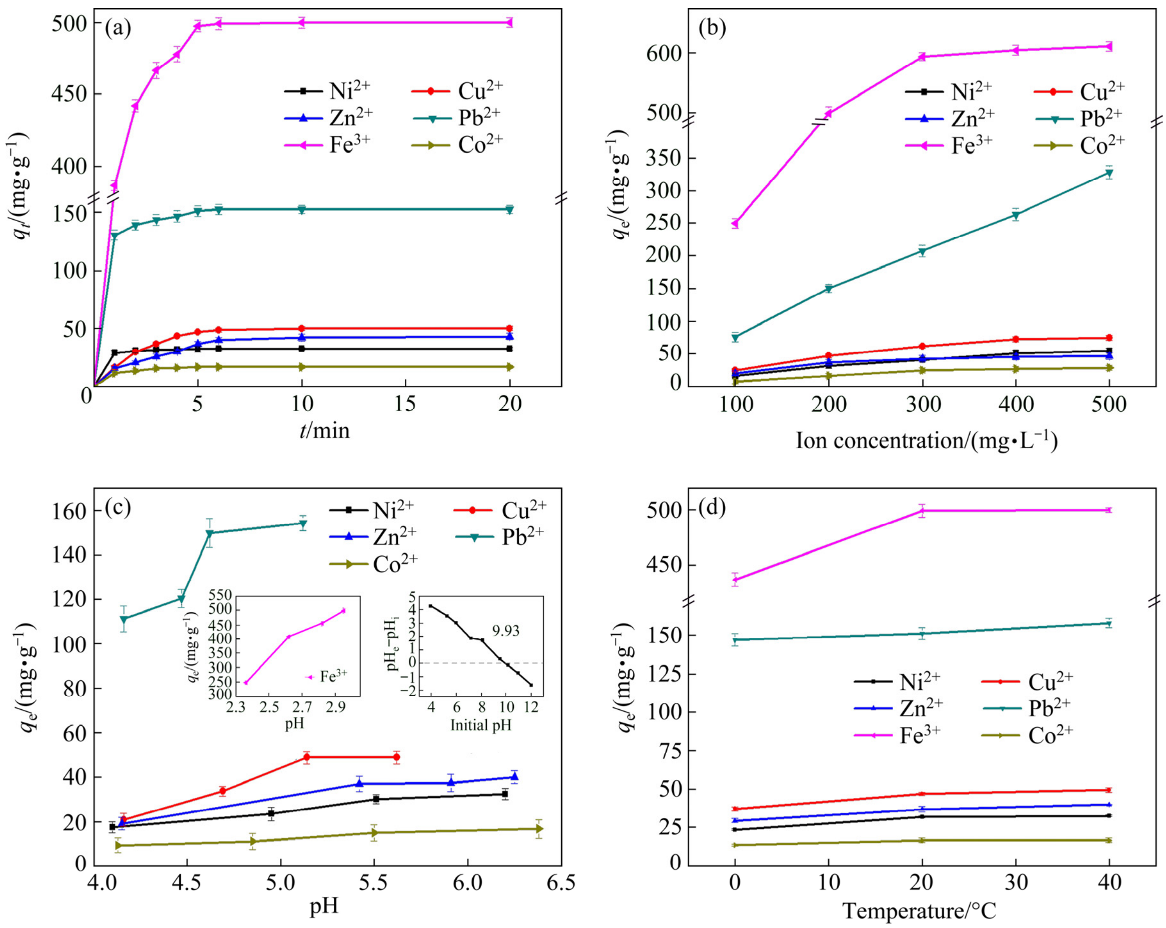

Fig. 6 Relationships between adsorption capacities of heavy metal ions and time (a), initial ions concentration (b), pH (c) and temperature (d)

of flower-like $Mg(OH)_2$ for Ni^{2+}, Cu^{2+}, Zn^{2+}, Pb^{2+}, Fe^{3+} and Co^{2+} against the initial ion concentration were also preliminary discussed, as presented in Fig. 6(b). It is obvious that the adsorption capacities increase along with the increase of the initial ion concentration, but the increase tapers off. This could be attributed to the increase in initial ion concentration making the equilibrium shift to the side with less ion concentration. However, the available active sites of the flower-like $Mg(OH)_2$ are constant at a given dosage and temperature.

3.3.3 Influence of pH value

The pH, as an important factor affecting the adsorption was also investigated. The adsorption capacities increase along with the increase of the pH (Fig. 6(c)), and they basically reach the maximums at a pH value of 5.14 for Cu^{2+} (initial pH) and about 5.50 for Ni^{2+}, Zn^{2+} and Co^{2+}. The adsorption capacity for Cu^{2+} has no obvious change in the pH range of 5.14−5.62. However, a continuous increase is observed for Pb^{2+} and Fe^{3+}. This may be related to the reactions with the releasing OH^-. The pH_{zpc} of flower-like $Mg(OH)_2$ is 9.93. At the pH value below the pH_{zpc}, two possible mechanisms for adsorption are ion-exchange and surface interaction. The high pH_{zpc} indicated that $Mg(OH)_2$ would be positively charged over the experimental pH range, the same as the metal ions. Thus, the ion-exchange is the main adsorption mechanism [21−23]. The dissolution of $Mg(OH)_2$ and neutralization at a low pH value have a negative effect on the adsorption. Hence, increasing pH value of the solution is beneficial to the adsorption. When the pH value increases from 5.91 to 6.25, an increase of adsorption capacity for Zn^{2+} is observed. One interpretation is that Zn^{2+} is dominant in experimental pH range with the presence of other Zn^{2+} species ($Zn(OH)^+$, $Zn(OH)_2$, and $Zn(OH)_3^-$). An increase in pH decreases Zn^{2+} content and even precipitates Zn^{2+} as $Zn(OH)_2$, resulting in an increase in removal [24,25].

3.3.4 Influence of temperature

The effect of temperature on the adsorption was also carried out at temperatures ranging from 273 to 313 K and initial pH values in 6 min, as shown in Fig. 6(d). The adsorption capacities increase with temperature rising, indicating the endothermic nature of the adsorption. Increasing temperature is favorable to the adsorption.

3.4 Adsorption mechanism

3.4.1 Adsorption isotherms

The experimental adsorption data at 20 °C were fitted by the Langmuir and Freundlich models, and the Langmuir isotherm is shown in Fig. 7. The parameters determined from the two models are listed in Table 1.

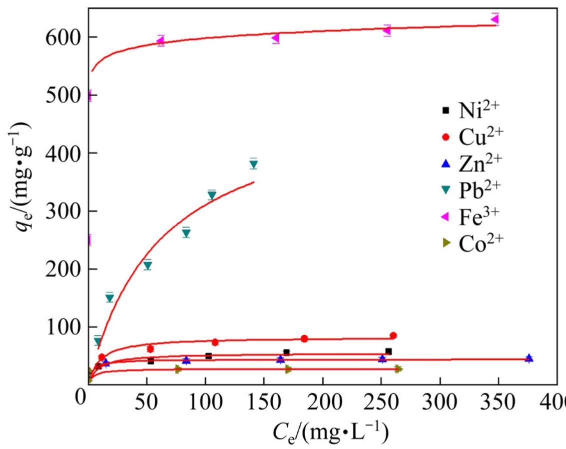

Fig. 7 Fitting of adsorption equilibrium data using Langmuir model

Maximum experimental adsorption capacities (Exp q_{max}) (55.14, 83.23, 44.86, 458.74, 609.65 and 28.25 mg/g for Ni^{2+}, Cu^{2+}, Zn^{2+}, Pb^{2+}, Fe^{3+} and Co^{2+}, respectively) are closely in agreement with those obtained from Langmuir isotherm (58.55, 85.84, 44.94, 485.44, 625.00 and 27.86 mg/g, respectively). And the higher correlation coefficients (R^2) fitted by the Langmuir model are observed except for Pb^{2+}. This confirms that the adsorption is well fitted by the Langmuir model, indicating that the adsorption takes place as monolayer. On the other hand, although the Freundlich model is inferior to the Langmuir model, the values of $1/n$ less than 1 confirms that adsorption is easy to achieve.

The adsorption capacities of the six heavy metal ions studied on different adsorbents are compared in Table 2. Although some adsorbents have higher adsorption capacity for certain ions, such as $Mg(OH)_2$/GO for Ni^{2+}, Cu^{2+}, Zn^{2+} and Pb^{2+}, MCs@Mg/Fe−LDHs for Cu^{2+} and Pb^{2+} and

Table 1 Langmuir and Freundlich model parameters for adsorption of heavy metal ions

Ion	Exp q_{max}/(mg·g^{-1})	Langmuir model			Freundlich model		
		q_{max}/(mg·g^{-1})	K_L/(L·mg^{-1})	R^2	K_F/(mg$^{1-1/n}$·g^{-1}·L$^{1/n}$)	$1/n$	R^2
Ni^{2+}	55.14	58.55	0.091	0.9910	20.832	0.183	0.9760
Cu^{2+}	83.23	85.84	0.087	0.9912	29.108	0.192	0.9864
Zn^{2+}	44.86	44.94	0.293	0.9997	31.517	0.061	0.9804
Pb^{2+}	458.74	485.44	0.020	0.9160	26.533	0.535	0.9652
Fe^{3+}	609.65	625.00	0.308	0.9985	519.507	0.031	0.9710
Co^{2+}	28.25	27.86	1.402	0.9997	23.358	0.032	0.9474

Table 2 Comparison of adsorption capacity for heavy metal ions by various adsorbents

Adsorbent	Time/min	q_e/(mg·g^{-1})						Ref.
		Ni^{2+}	Cu^{2+}	Zn^{2+}	Pb^{2+}	Fe^{3+}	Co^{2+}	
$Fe(OH)_3$ MS	80				75.64			[26]
$Mg(OH)_2$/GO	1440	175.0	216.0	327.7	344.4			[27]
Mg−Al−D2EHPA	60		68.66					[28]
Ni@$Mg(OH)_2$	50		40.18	36.11				[29]
MCs@Mg/Fe−LDHs	1440		338.98		755.27			[30]
MgAl−LDH@RHB	1440		104.34					[31]
MCC−$Mg(OH)_2$	50						153.84	[32]
CaAl−LDH	600		122.7		221.2			[33]
Mn_3O_4/TiO_2 sheets	60					69.80		[34]
YNU-1 nanobelts	720					456.37		[35]
Phosphate	1440	93.90	50.84	91.57	124.32		123.75	[36]
Hydroxyapatite	1440	4.34	7.37	0.92	26.52		0.59	[37]
Flower-like $Mg(OH)_2$	6	58.55	85.84	44.94	485.44	625.00	27.86	This work

MCC−$Mg(OH)_2$ for Co^{2+}, flower-like $Mg(OH)_2$ exhibits a satisfactory adsorption for all six ions and has high efficiency. The rapid and efficient removal of heavy metal ions is its advantage.

3.4.2 Adsorption thermodynamics

To assess the spontaneity of the adsorption, the thermodynamic parameters were calculated and the results are displayed in Table 3. The positive values of $\Delta H^{\ominus}$ and $\Delta S^{\ominus}$ reveal that the adsorption is endothermic and the disorderness of solid−liquid interfaces is elevated [11−15,38]. Negative values of $\Delta G^{\ominus}$ ranging from −6.182 to −16.485 kJ/mol imply that the adsorption process is spontaneous. Further, with increasing the temperature, the values of $\Delta G^{\ominus}$ is more negative, suggesting that higher temperature is in favor of the adsorption.

3.4.3 Adsorption kinetics

The adsorption data were fitted by the pseudo-first-order, pseudo-second-order and intra-particle diffusion kinetic models. The fitting results of adsorption data by the pseudo-second-order and intra-particle diffusion kinetic models are displayed in Fig. 8 and Fig. 9, respectively. The relevant parameters of the pseudo-first/second-order models are listed in Table 4. It could be seen that the pseudo-second-order model fits the adsorption data better owning to the higher correlation coefficients (R^2). Moreover, equilibrium adsorption capacities (q_e) are closer to experimental results (q_{exp}) of 32.72, 64.81, 47.94, 154.56, 524.22 and 17.48 mg/g for Ni^{2+}, Cu^{2+}, Zn^{2+}, Pb^{2+}, Fe^{3+} and Co^{2+}, respectively. Thus, the adsorption process involves chemisorption, which is consistent with the adsorption isotherms since chemisorption is usually monolayer [13,14].

Table 3 Thermodynamic parameters for adsorption of heavy metal ions

T/K	Ion	$\Delta G^{\ominus}$/(kJ·mol^{-1})	$\Delta H^{\ominus}$/(kJ·mol^{-1})	$\Delta S^{\ominus}$/(kJ·K^{-1}·mol^{-1})
273		−7.679		
293	Ni^{2+}	−8.385	1.953	0.035
313		−9.042		
273		−8.247		
293	Cu^{2+}	−9.458	8.273	0.061
313		−10.107		
273		−7.119		
293	Zn^{2+}	−9.105	19.988	0.099
313		−9.861		
273		−11.378		
293	Pb^{2+}	−12.406	2.684	0.052
313		−13.267		
273		−14.245		
293	Fe^{3+}	−15.402	1.537	0.058
313		−16.485		
273		−6.182		
293	Co^{2+}	−6.874	3.625	0.035
313		−7.436		

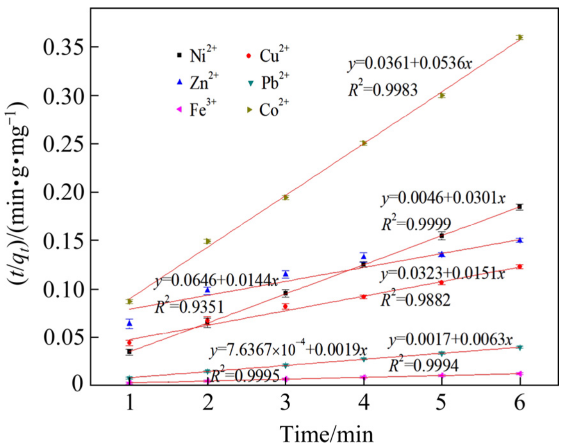

Fig. 8 Pseudo-second-order model plots for adsorption of heavy metal ions on $Mg(OH)_2$

The fitting lines do not pass through the origin point and a multi-linearity relationship is observed in Fig. 9. It is well known that the higher the intercept is, the greater the boundary layer effect is. Rapid adsorption is observed within the initial 1 min, and thereafter the adsorption rate decreases. That is to say, an instantaneous boundary (film) diffusion occurs in the initial 1 min, which may be related to the mass transfer of heavy metal ions from bulk solution to the surface of flower-like $Mg(OH)_2$ [14]. During the second step, the adsorption rates of Ni^{2+}, Pb^{2+}, Fe^{3+} and Co^{2+} decrease obviously, but the decrease is unapparent for Cu^{2+} and Zn^{2+}. In the last step, the final equilibrium is reached. The adsorption might be shifted from intra-particle diffusion to surface adsorption [6]. The overall adsorption rate is simultaneously controlled by boundary (film) diffusion and intra-particle diffusion [13]. However, an exception is observed as the adsorption rate of Zn^{2+} increases, which is different from previous reports [11,22−24]. One possible explanation is that Mg^{2+} and OH^- are

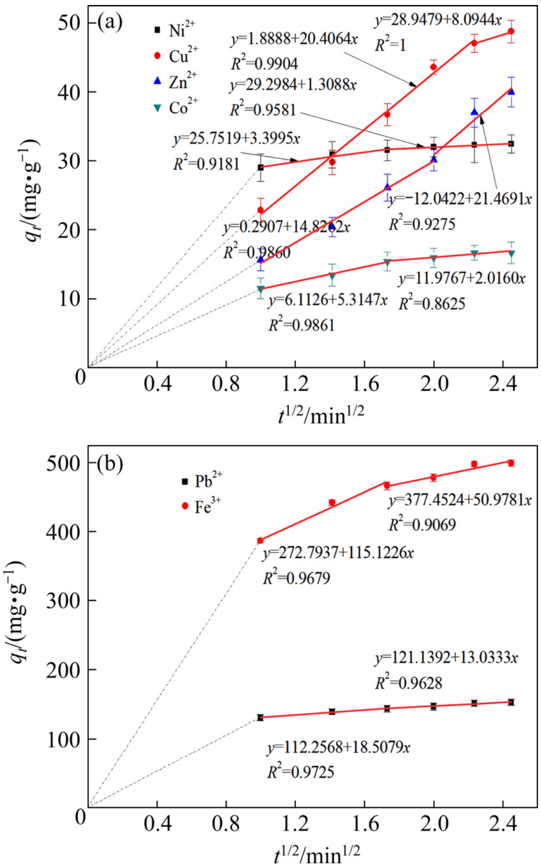

Fig. 9 Intra-particle diffusion kinetics for adsorption of heavy metal ions on $Mg(OH)_2$: (a) Ni^{2+}, Cu^{2+}, Zn^{2+} and Co^{2+}; (b) Pb^{2+} and Fe^{3+}

released from $Mg(OH)_2$ during adsorption. The ion-exchange happens easily between Mg^{2+} and Zn^{2+} owning to the proximate ionic radii (0.72 nm of Mg^{2+} and 0.74 nm of Zn^{2+}) [25]. With the increase of solution pH, Zn^{2+} is still dominant, but Zn^{2+} concentration decreases. The concentrations of other Zn^{2+} species, such as $Zn(OH)^+$, $Zn(OH)_2$ and $Zn(OH)_3^-$, increase. Thus, Zn^{2+} adsorption may involve multiple Zn^{2+} species rather than a single Zn^{2+}, which may enhance the adsorption rate [24].

Table 4 Kinetic parameters for adsorption of heavy metal ions

Ion	Pseudo-first-order			Pseudo-second-order		
	$q_e/(mg\cdot g^{-1})$	k_1/min^{-1}	R^2	$q_e/(mg\cdot g^{-1})$	$k_2/(g\cdot mg^{-1}\cdot min^{-1})$	R^2
Ni^{2+}	29.42	0.4605	0.8072	32.72	0.2030	0.9999
Cu^{2+}	69.32	2.2739	0.9710	64.81	0.0074	0.9882
Zn^{2+}	49.44	7.2745	0.9299	47.94	0.0067	0.9351
Pb^{2+}	356.52	0.2518	0.9310	154.56	0.0246	0.9994
Fe^{3+}	246.22	2.5336	0.9036	524.22	0.0048	0.9995
Co^{2+}	27.82	0.0394	0.9983	17.48	0.0907	0.9983

3.4.4 FT-IR spectra and XRD patterns of $Mg(OH)_2$ before and after adsorption

The FT-IR spectra and XRD patterns of $Mg(OH)_2$ before and after adsorption are displayed in Fig. 10. The broad band located at 3436.88 cm^{-1} is due to O—H vibration from the absorbed H_2O. A sharp peak at 3699.10 cm^{-1} attributed to the stretching vibration of —OH is observed. The bands observed at 3646.59, 2923.26, 2853.63 and 1420.28 cm^{-1} are due to bending vibration of —OH. The peaks at 1643.60 and 1124.02 cm^{-1} are assigned to CO_3^{2-}, and the vibration peak around 2364.76 cm^{-1} is designated to the characteristic vibration of C═O bands, which are caused by CO_2 adsorption [39,40]. Also, the peak at 1643.60 cm^{-1} is due to the stretching vibration of —OH [40]. The weak adsorption band assigned to Mg—O bonds at 431.71 cm^{-1} is observed. The bands at 1643.60, 1420.28 and 1124.02 cm^{-1} are enhanced after adsorption, which is largely due to the CO_2 adsorption. However, the characteristic band of Mg—O at 441.77 cm^{-1} is weakened. XRD study reveals that $Mg(OH)_2$ adsorbent has no obvious change after adsorbing Ni^{2+}, Cu^{2+}, Zn^{2+} and Co^{2+}. But the variation is significant after adsorbing Pb^{2+} for the formation of $Pb_3(CO_3)_2(OH)_2$ due to CO_2 adsorption, which can account for the characteristic vibration of C═O bands and CO_3^{2-}. $Fe(OH)_3$ is observed after adsorption and the diffraction intensity decreases obviously due to the dissolution of $Mg(OH)_2$ in low pH solution.

Herein, the adsorption of the studied heavy metal ions on flower-like $Mg(OH)_2$ is schematically presented in Fig. 11. The adsorption of Ni^{2+}, Cu^{2+}, Zn^{2+} and Co^{2+} is mainly due to the ion-exchange interaction owning to the proximate ionic radii. As for Fe^{3+} and Pb^{2+}, the precipitation reactions should be the main factors.

3.4.5 Recyclability and cost analysis

The recyclability of the adsorbent is an important factor in reducing cost. Flower-like $Mg(OH)_2$ after adsorption of Ni^{2+}, Cu^{2+}, Zn^{2+} and Co^{2+} can be recovered by ammonia solution, and after 4 cycles, the adsorption capacities for these ions are only slightly reduced by 2%−5%. Further, the repeated recycling solution is used to recover the valuable metals. But as for $Mg(OH)_2$ after adsorption of Fe^{3+} and Pb^{2+}, hydrothermal recrystallization after sulfate acid dissolution may be a better option.

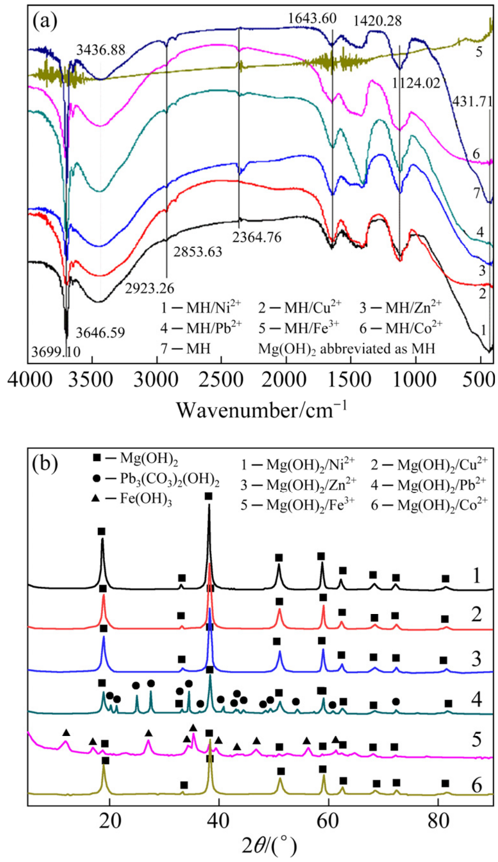

Fig. 10 FT-IR spectra (MH−$Mg(OH)_2$) (a) and XRD patterns (b) of $Mg(OH)_2$ before and after adsorption

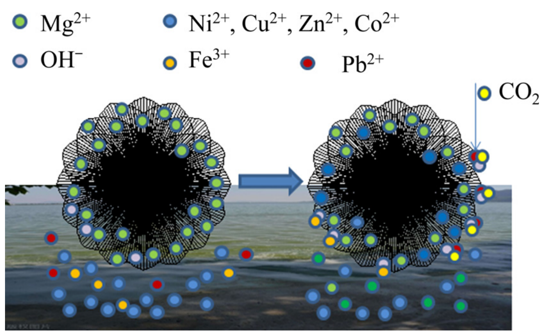

Fig. 11 Schematic diagram of adsorption of heavy metal ions on magnesium hydroxide

Fabrication of flower-like $Mg(OH)_2$ from $MgSO_4$ effluent has significant social benefit and environmental value. When taking into account of facile fabrication, rapid and efficient removal of heavy metal ions and recyclability, flower-like $Mg(OH)_2$ is a cost-effective candidate for the removal of heavy metal ions.

4 Conclusions

(1) The appropriate conditions for the

fabrication of spherical flower-like $Mg(OH)_2$ are Mg^{2+}/NH_4OH molar ratio of 0.5, temperature of 120 °C and time of 1 h at Mg^{2+} concentration of 2 mol/L.

(2) Spherical flower-like $Mg(OH)_2$ exhibits an excellent adsorption ability for heavy metal ions. At 20 °C, the adsorption equilibrium is reached in 6 min, and the maximum adsorption capacities for Ni^{2+}, Cu^{2+}, Zn^{2+}, Pb^{2+}, Fe^{3+} and Co^{2+} are 58.55, 85.84, 44.94, 485.44, 625.00 and 27.86 mg/g, respectively. The adsorption is well fitted by the Langmuir mode. The adsorption kinetics follows pseudo-second-order kinetic model. Chemisorption is the operative mechanism. Spherical flower-like $Mg(OH)_2$ is a qualified candidate for the removal of heavy metal ions.

Acknowledgments

This work was supported by the National Natural Science Foundation of China (Nos. 51774070 and 52004165), and the Science and Technology Project of Yunnan Province, China (No. 202101AS070029).

References

[1] HAMDY M S, AWWAD N S, ALSHAHRANI A M. Mesoporous magnesia: Synthesis, characterization, adsorption behavior and cytotoxic activity [J]. Materials & Design, 2016, 110: 503−509.

[2] JING Qing-xiu, WANG Yun-yan, CHAI Li-yuan, TANG Chong-jian, HUANG Xiao-dong, GUO Huan, WANG Wei, YOU Wei. Adsorption of copper ions on porous ceramsite prepared by diatomite and tungsten residue [J]. Transactions of Nonferrous Metals Society of China, 2018, 28(5): 1053−1060.

[3] FENG J, ZOU L Y, WANG Y T, LI B W, HE X F, FAN Z J, REN Y M, LV Y Z, ZHANG M L, CHEN D. Synthesis of high surface area, mesoporous MgO nanosheets with excellent adsorption capability for Ni(II) via a distillation treating [J]. Journal of Colloid and Interface Science, 2015, 438: 259–267.

[4] ZHAO Yue, CHEN Hui, YAN Qun. Enhanced phosphate removal during the simultaneous adsorption of phosphate and Ni^{2+} from electroless nickel wastewater by calcium silicate hydrate (CSH) [J]. Environmental Technology & Innovation, 2017, 8: 141–149.

[5] SHEN Xiao-yi, SHAO Hong-mei, LIU Yan, ZHAI Yu-chun. Synthesis and photocatalytic performance of ZnO with flower-like structure from zinc oxide ore [J]. Journal of Materials Science & Technology, 2020, 51: 1−7.

[6] LIU Meng-di, XU Jing, CHENG Bei, HO Wing-kei, YU Jia-guo. Synthesis and adsorption performance of $Mg(OH)_2$ hexagonal nanosheet−grapheme oxide composites [J] Applied Surface Science, 2015, 332: 121−129.

[7] WANG Qiang, LI Chun-hong, GUO Ming, SUN Ling-na, HU Chang-wen. Hydrothermal synthesis of hexagonal magnesium hydroxide nanoflakes [J]. Materials Research Bulletin, 2014, 51: 35−39.

[8] ZHENG Jun, ZHOU Wei. Solution-phase synthesis of magnesium hydroxide nanotubes [J]. Materials Letters, 2014, 127: 17−19.

[9] HOSAIN A N A, NEMR A E, SIKAILY A E, MAHMOUD M E, AMIRA M F. Surface modifications of nanochitosan coated magnetic nanoparticles and their applications in Pb(II), Cu(II) and Cd(II) removal [J]. Journal of Environmental Chemical Engineering, 2020, 8: 104316.

[10] WANG Yun-yan, YAO Wen-bin, WANG Qing-wei, YANG Zhi-hui, LIANG Li-fen, CHAI Li-yuan. Synthesis of phosphate-embedded calcium alginate beads for Pb(II) and Cd(II) sorption and immobilization in aqueous solutions [J]. Transactions of Nonferrous Metals Society of China, 2016, 26(8): 2230−2237.

[11] HUANG Ji-quan, CAO Yong-ge, LIU Zhu-guang, DENG Zhong-hua, TANG Fei, WANG Wen-chao. Efficient removal of heavy metal ions from water system by titanate nanoflowers [J]. Chemical Engineering Journal, 2012, 180: 75−80.

[12] PIRMORADI M, HASHEMIAN S, SHAYESTEH M R. Kinetics and thermodynamics of cyanide removal by ZnO@NiO nanocrystals [J]. Transactions of Nonferrous Metals Society of China, 2017, 27(6): 1394−1403.

[13] JUNG K W, LEE S Y, CHOI J W, LEE Y J. A facile one-pot hydrothermal synthesis of hydroxyapatite/biochar nano-composites: Adsorption behavior and mechanisms for the removal of copper(II) from aqueous media [J]. Chemical Engineering Journal, 2019, 369: 529−541.

[14] VENKATESHA T G, ARTHOBA N Y, CHETHANA B K. Adsorption of Ponceau S from aqueous solution by MgO nanoparticles [J]. Applied Surface Science, 2013, 276: 620−627.

[15] WANG Zhang-hong, SHEN De-kui, SHEN Fei, WU Chun-fei, GU Sai. *Ginkgo biloba* L. shells-based adsorbent for the removal of Cu^{2+} and Cd^{2+} from aqueous solution: Kinetics, isotherm, thermodynamics and mechanisms [J]. Journal of Molecular Liquids, 2017, 241: 603−611.

[16] LIMA E C, HOSSEINI-BANDEGHARAEI A, MORENO-PIRAJÁN J C, ANASTOPOULOS I. A critical review of the estimation of the thermodynamic parameters on adsorption equilibria. Wrong use of equilibrium constant in the Van't Hoof equation for calculation of thermodynamic parameters of adsorption [J]. Journal of Molecular Liquids, 2019, 273: 425−434.

[17] IVANETS A I, SRIVASTAVA V, KITIKOVA N V, SHASHKOVA I L, SILLANPÄÄ M. Kinetic and thermodynamic studies of the Co(II) and Ni(II) ions removal from aqueous solutions by Ca−Mg phosphates [J]. Chemosphere, 2017, 171: 348−354.

[18] LAN Sheng-jie, LI Li-juan, XU De-fang, ZHU Dong-hai, LIU Zhi-qi, NIE Feng. Surface modification of magnesium hydroxide using vinyltriethoxysilane by dry process [J]. Applied Surface Science, 2016, 382: 56−62.

[19] CHEN Yong-bin, ZHOU Tao, FANG Hua-xiong, LI Si-min,

YAO Yu-ting, FAN Bai-lin, WANG Jian. A novel preparation of nanosized hexagonal $Mg(OH)_2$ as a flame retardant [J]. Particuology, 2016, 24: 177−182.

[20] LV Ying, ZHANG Zhi-an, LAI Yan-qing, LI Jie, LIU Ye-xiang. Formation mechanism for planes (011) and (001) oriented $Mg(OH)_2$ films electrodeposited on SnO_2 coating glass [J]. CrystEngComm, 2011, 13(11): 3848−3851.

[21] HUANG Qi-qi, CHEN Yan, YU Hai-qin, YAN Liang-guo, ZHANG Jing-he, WANG Ben, DU Bin, XING Li-ting. Magnetic graphene oxide/MgAl-layered double hydroxide nanocomposite: One-pot solvothermal synthesis, adsorption performance and mechanisms for Pb^{2+}, Cd^{2+}, and Cu^{2+} [J]. Chemical Engineering Journal, 2018, 341: 1−9.

[22] YU Jia-nan, ZHU Zhi-liang, ZHANG Hua, QIU Yan-ling, YIN Da-qiang. Mg−Fe layered double hydroxide assembled on biochar derived from rice husk ash: facile synthesis and application in efficient removal of heavy metals [J]. Environmental Science and Pollution Research, 2018, 25: 24293−24304.

[23] ZHAO Shi-feng, MENG Zi-lin, FAN Xin, JING Rui-sen, YANG Jun-shan, SHAO Yi-fei, LIU Xi-juan, WU Mi, ZHANG Qian, LIU Ai-ju. Removal of heavy metals from soil by vermiculite supported layered double hydroxides with three-dimensional hierarchical structure [J]. Chemical Engineering Journal, 2020, 390: 124554.

[24] CALISKAN N, KUL A R, ALKAN S, SOGUT E G, ALACABEY I. Adsorption of zinc(II) on diatomite and manganese-oxide-modified diatomite: A kinetic and equilibrium study [J]. Journal of Hazardous Materials, 2011, 193: 27−36.

[25] ZHAO Zheng-fu, ZHANG Xian, ZHOU Hong-jian, LIU Gang, KONG Ming-guang, WANG Guo-zhong. Microwave-assisted synthesis of magnetic Fe_3O_4−mesoporous magnesium silicate core−shell composites for the removal of heavy metal ions [J]. Microporous and Mesoporous Materials, 2017, 242: 50−58.

[26] ZHAO Xiao-le, SU Ying-chun, LI Shu-bin, BI Ya-jun, HAN Xiao-jun. A green method to synthesize flowerlike $Fe(OH)_3$ microspheres for enhanced adsorption performance toward organic and heavy metal pollutants [J]. Journal of Environmental Science, 2018, 73: 47−57.

[27] WANG Pan-pan, YE Yi-xing, LIANG De-wei, SUN Hong-mei, LIU Jun, TIAN Zhen-fei, LIANG Chang-hao. Layered mesoporous $Mg(OH)_2$/GO nanosheet composite for efficient removal of water contaminants [J]. RSC Advances, 2016, 6: 26977−26983.

[28] ROUAHNA N, BARKAT D, OUAKOUAK A, SRASRA E. Synthesis and characterization of Mg−Al layered double hydroxide intercalated with D2EHPA: Application for copper ions removal from aqueous solution [J]. Journal of Environmental Chemical Engineering, 2018, 6: 1226−1232.

[29] ZHANG Meng, SONG Wei-qiang, CHEN Qiu-ling, MIAO Bao-ji, HE Wei-chun. One-pot synthesis of magnetic Ni@$Mg(OH)_2$ core−shell nanocomposites as a recyclable removal agent for heavy metals [J]. ACS Applied Materials & Interfaces, 2015, 7: 1533−1540.

[30] XIE Yuan-yuan, YUAN Xing-zhong, WU Zhi-bin, ZENG Guang-ming, JIANG Long-bo, PENG Xin, LI Hui. Adsorption behavior and mechanism of Mg/Fe layered double hydroxide with Fe_3O_4−carbon spheres on the removal of Pb(II) and Cu(II) [J]. Journal of Colloid and Interface Science, 2019, 536: 440−445.

[31] LI An-yu, ZHANG Yue, GE Wen-zhan, ZHANG Yu-tong, LIU Li-hu, QIU Guo-hong. Removal of heavy metals from wastewaters with biochar pyrolyzed from MgAl-layered double hydroxide-coated rice husk: Mechanism and application [J]. Bioresource Technology, 2022, 347: 126425.

[32] WANG Rui-feng, DENG Li-gao, FAN Xue-jing, LI Kai, LU Hai-qin, LI Wen. Removal of heavy metal ion cobalt(II) from wastewater via adsorption method using microcrystalline cellulose-magnesium hydroxide [J]. International Journal of Biological Macromolecules, 2021, 189: 607−617.

[33] YAO Wen, WANG Jian, WANG Peng-yi, WANG Xiang-xue, YU Shu-jun, ZOU Yi-dong, HOU Jing, HAYAT T, ALSAEDI A, WANG Xiang-ke. Synergistic coagulation of GO and secondary adsorption of heavy metal ions on Ca/Al layered double hydroxides [J]. Environmental Pollution, 2017, 229: 827−836.

[34] KHAN S B, RAHMAN M M, MARWANI H M, ASIRI A M, ALAMRY K A, RUB M A. Selective adsorption and determination of iron(III): Mn_3O_4/TiO_2 composite nanosheets as marker of iron for environmental applications [J]. Applied Surface Science, 2013, 282: 46−51.

[35] FAN Wen-wen, LIU Xiao-lan, CHENG Yi, QIN Yu, YANG Shao-xiong, LU Zhi-xiang, LIU Yan-xiong, CAO Qiu-e, ZHENG Li-yan. Two-dimensional metal-organic framework nanobelts for selective Fe^{3+} removal from aqueous solution with high adsorption capacity [J]. Separation and Purification Technology, 2020, 239: 116559.

[36] IVANETS A, KITIKOVA N, SHASHKOVA I, MATRUNCHIK Y, KUL'BITSKAYA L, SILLANPÄÄ M. Non-acidic synthesis of phosphatized dolomite and its sorption behaviour towards Pb^{2+}, Zn^{2+}, Cu^{2+}, Cd^{2+}, Ni^{2+}, Sr^{2+} and Co^{2+} ions in multicomponent aqueous solution [J]. Environmental Technology & Innovation, 2016, 6: 152−164.

[37] IVANETS A I, KITIKOVA N V, SHASHKOVA I L, ROSHCHINA M Y, SRIVASTAVA V, SILLANPÄÄ M. Adsorption performance of hydroxyapatite with different crystalline and porous structure towards metal ions in multicomponent solution [J]. Journal of Water Process Engineering, 2019, 32: 100963.

[38] KARANAC M, ĐOLIĆ M, VELJOVIĆ Đ, RAJAKOVIĆ-OGNJANOVIĆ V, VELIČKOVIĆ Z, PAVIĆEVIĆ V, MARINKOVIĆ A. The removal of Zn^{2+}, Pb^{2+}, and As(V) ions by lime activated fly ash and valorization of the exhausted adsorbent [J]. Waste Management, 2018, 78: 366−378.

[39] DAS P S, BAKULI S, SAMANTA A, MANDAL A K, GHOSH J, DEYAND A, MUKHOPADHYAY A K. Very high Cu(II) adsorption efficacy of designed nano-platelet $Mg(OH)_2$ assembly [J]. Materials Research Express, 2017, 4(2): 025025.

[40] SHAFIQ M, ALAZBA A A, AMIN M T. Adsorption of divalent copper ions from synthetic wastewater using layered double hydroxides (NiZnFe) and its composites with banana biochar and carbon nanotubes [J]. Water Air Soil Pollution, 2020, 231: 346.

花球状 $Mg(OH)_2$ 的制备及其对重金属离子的快速高效去除

申晓毅[1,2]，黄彦翔[1]，邵鸿媚[3]，王 媛[1]，韩 庆[1]，陈建设[1]，李斌川[1]，翟玉春[1]

1. 东北大学 冶金学院 多金属共生矿生态化冶金教育部重点实验室，沈阳 110819；
2. 东北大学 辽宁省冶金传感器及技术重点实验室，沈阳 110819；
3. 沈阳理工大学 环境与化学工程学院，沈阳 110159

摘　要：由 $MgSO_4$ 废液制备球形花状 $Mg(OH)_2$，并评估其对重金属离子的吸附性能。合适的制备条件为 Mg^{2+}浓度 2 mol/L、Mg^{2+}/NH_4OH 摩尔比 1:0.5、温度 120 ℃和时间 1 h。由超薄片组成的球形花状 $Mg(OH)_2$ 对重金属离子具有良好的吸附能力，6 min 即可达到吸附平衡。20 ℃时 $Mg(OH)_2$ 对 Ni^{2+}、Cu^{2+}、Zn^{2+}、Pb^{2+}、Fe^{3+}和 Co^{2+}的最大吸附量分别为 58.55、85.84、44.94、485.44、625.00 和 27.86 mg/g。吸附过程符合 Langmuir 模型，为单分子层吸附。吸附动力学符合准二级动力学模型，化学吸附是其作用机制。球形花状 $Mg(OH)_2$ 是合格的重金属离子吸附材料。

关键词：$MgSO_4$ 废液；花状 $Mg(OH)_2$；重金属离子；吸附

(Edited by Bing YANG)